

# Targetless LiDAR-Camera Calibration with Neural Gaussian Splatting

Haebeom Jung<sup>1</sup>, Namtae Kim<sup>1</sup>, Jungwoo Kim<sup>2</sup>, and Jaesik Park<sup>1</sup>

**Abstract**— Accurate LiDAR-camera calibration is crucial for multi-sensor systems. However, traditional methods often rely on physical targets, which are impractical for real-world deployment. Moreover, even carefully calibrated extrinsics can degrade over time due to sensor drift or external disturbances, necessitating periodic recalibration. To address these challenges, we present a Targetless LiDAR-Camera Calibration (TLC-Calib) that jointly optimizes sensor poses with a neural Gaussian-based scene representation. Reliable LiDAR points are frozen as anchor Gaussians to preserve global structure, while auxiliary Gaussians prevent local overfitting under noisy initialization. Our fully differentiable pipeline with photometric and geometric regularization achieves robust and generalizable calibration, consistently outperforming existing targetless methods on KITTI-360, WAYMO, and FAST-LIVO2, and surpassing even the provided calibrations in rendering quality.

## I. INTRODUCTION

Recent advances in Novel View Synthesis (NVS) have enabled increasingly sophisticated reconstruction of 3D scenes from 2D images. In particular, the emergence of Neural Radiance Fields (NeRF) [1] and 3D Gaussian Splatting (3DGS) [2] has significantly improved rendering fidelity, with 3DGS additionally offering faster rendering than earlier approaches [3], [4]. Despite these innovations, achieving higher rendering quality and precise 3D geometry often requires multi-sensor fusion, such as the integration of LiDAR and multiple cameras. This complementary fusion provides richer and more accurate spatial information, and recent studies [5], [6] have reported substantial performance gains, especially in NVS tasks.

However, neural rendering techniques in multi-sensor setups rely heavily on accurate knowledge of each sensor’s mounting position and orientation, commonly referred to as sensor extrinsics. These parameters are not necessarily static, and even slight mechanical vibrations, thermal expansion, or physical impacts can cause subtle shifts in sensor positioning over time, leading to misalignment and necessitating periodic recalibration.

Target-based calibration methods [7]–[9] are widely adopted as a standard solution. For instance, placing checkerboard patterns or spherical reflectors within the shared field of view enables accurate pose estimation. While effective, this approach can require costly infrastructure or large-scale target installations, especially in systems with multiple sensors or

<sup>1</sup>H. Jung, N. Kim, and J. Park are with the Department of Interdisciplinary Program in Artificial Intelligence, Seoul National University, Seoul, S. Korea [haebeom.jung, knt0613, jaesik.park]@snu.ac.kr

<sup>2</sup>J. Kim is with the Department of Artificial Intelligence, Yonsei University, Seoul, S. Korea jungwkim@yonsei.ac.kr

wide baselines. Moreover, even carefully calibrated target-based methods often struggle to align LiDAR and camera data at far distances, limiting their utility in real-world scenarios.

By contrast, targetless methods [10]–[12] calibrate sensors using only raw sensor data, leveraging environmental features such as planes or edges [12]. These methods eliminate the need for physical targets, but face significant challenges due to the intrinsic differences between LiDAR and camera modalities, particularly the sparsity of LiDAR point clouds. Deep learning-based approaches [13], [14] attempt to bridge this gap, but typically require large labeled datasets and often struggle to generalize to new sensor configurations or scenes. In the NVS domain, recent efforts have integrated LiDAR data into NeRF-based pipelines [15], [16]. Although these NeRF-based methods [17]–[19] can jointly optimize scene representations and sensor poses, their implicit volumetric nature results in high computational overhead, often scaling with the number of images.

In contrast, we adopt a neural Gaussian representation for efficient and scalable optimization. We propose *TLC-Calib*, a Targetless LiDAR-Camera Calibration framework based on neural Gaussian representations. By leveraging differentiable rendering, it jointly optimizes sensor extrinsics and scene representation without relying on explicit targets or external supervision. To enhance stability, reliable LiDAR points are designated as anchor Gaussians to preserve global structure, while auxiliary Gaussians mitigate local overfitting, particularly under inaccurate initial poses. This design enables robust optimization even with noisy initialization and improves alignment quality across diverse scenes, including public datasets where the provided extrinsics are often suboptimal (see Fig. 1).

The primary contributions of this work are as follows:

- We stabilize global scale and translation by designating reliable LiDAR points as anchor Gaussians to preserve the overall structure, and by introducing auxiliary Gaussians to regularize local geometry under challenging initialization parameters.
- We combine photometric loss with scale-consistent geometric constraints, enabling robust alignment of LiDAR and camera sensors across diverse environments and trajectories.
- We validate our approach on three real-world setups, including two autonomous driving datasets and one handheld setup with a solid-state LiDAR, demonstrating strong generalization and high calibration accuracy. The estimated extrinsics also provide improved rendering quality over the dataset-provided calibrations.

## II. RELATED WORK

### A. Targetless Sensor Calibration

Targetless calibration methods align sensors using environmental cues instead of physical markers. Edge-based approaches [10], [20], [21] extract geometric edges from point clouds and images to estimate sensor extrinsics. In parallel, learning-based approaches have also been actively studied. RegNet [13] employs convolutional neural networks to predict extrinsic parameters between LiDAR scans and images, while LCCNet [14] improves upon this by introducing a cost volume for more robust estimation. Additionally, segmentation-based methods maximize overlap regions [22], align object edges [23], or leverage SAM-based masks for calibration [24]. However, the accuracy of such methods is often limited by the quality of segmentation.

### B. Neural Rendering Pose Optimization

NeRF [1] and 3DGS [2] have been extended to refine camera poses and scene geometry jointly. NeRFmm [25] introduced a photometric loss for pose optimization, and SC-NeRF [26] jointly optimized intrinsics and poses. NoPose-NeRF [27] and CF-3DGS [28] further leverage monocular depth cues to improve accuracy. NoPoseGS [29] achieves faster convergence by extending the high-performance CUDA rendering kernel. However, extending these approaches to multi-sensor systems is nontrivial due to scale inconsistency and modality gaps between LiDAR and camera data. As a result, existing methods remain limited to camera-only systems and cannot be directly applied to heterogeneous sensor fusion.

### C. Neural Rendering Sensor Calibration

Recently, neural rendering has been explored for sensor extrinsic calibration. INF [17] trains a density network from LiDAR scans to calibrate extrinsics via radiance fields. MOISST [18] jointly handles temporal misalignment and calibration. UniCal [19] incorporates surface alignment and correspondence constraints, though its reliance on feature-based registration limits generality. Despite their effectiveness, these NeRF-based approaches suffer from long training times.

To accelerate optimization, 3DGS has recently been adopted for calibration. 3DGS-Calib [30] leverages LiDAR points as 3D Gaussian references for efficient calibration but represents the scene with hash-grid encoding [31], which is sensitive to scene complexity and hyperparameters. Concurrent work, RobustCalibration [32], employs 2DGS to learn geometric constraints from LiDAR point clouds, but both approaches remain restricted to LiDAR-observed regions. In contrast, TLC-Calib introduces anchor and auxiliary Gaussians that extend calibration beyond LiDAR-overlapped regions and form a fully differentiable representation, enabling robust and generalizable calibration across diverse environments.

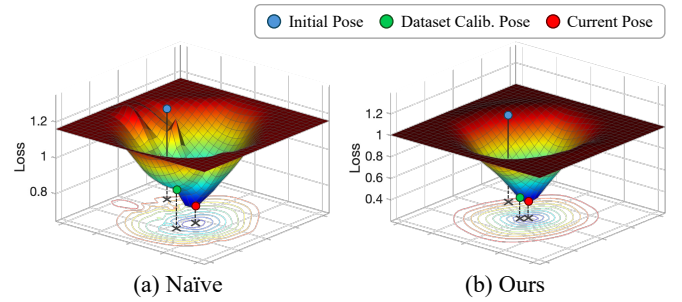


Fig. 1: Comparison of optimization landscapes. (a) Our naïve attempt (3DGS [2] + camera rig optimization) appears to converge to a global minimum within its own loss landscape, but the landscape is ambiguous and misaligned with the true geometry, leading to convergence to an incorrect pose far from the dataset calibration. (b) Our method produces a smoother and more geometrically consistent landscape by leveraging anchor and auxiliary Gaussians, enabling stable convergence toward the correct pose closer to the dataset calibration and demonstrating more reliable optimization behavior.

## III. PRELIMINARY

### A. 3D Gaussian Splatting

3D Gaussian Splatting has emerged as an effective representation for NVS by modeling a scene as a collection of 3D Gaussians. Each Gaussian  $\mathbf{G}_i$  is parameterized by its center  $\boldsymbol{\mu}_i \in \mathbb{R}^3$ , an anisotropic covariance matrix  $\boldsymbol{\Sigma}_i \in \mathbb{R}^{3 \times 3}$ , an opacity  $\alpha_i \in [0, 1]$ , and spherical harmonics coefficients  $\mathbf{c}_i$  for view-dependent color. In the world coordinate system, the spatial extent of each Gaussian is represented by a density function. To ensure that the covariance matrix  $\boldsymbol{\Sigma}_i$  remains positive semi-definite, it is decomposed into a rotation matrix  $\mathbf{R}_i \in \text{SO}(3)$  and a diagonal scale matrix  $\mathbf{S}_i \in \mathbb{R}^{3 \times 3}$  as follows:

$$\mathbf{G}_i(\mathbf{x}) = e^{-\frac{1}{2}(\mathbf{x} - \boldsymbol{\mu}_i)^\top \boldsymbol{\Sigma}_i^{-1}(\mathbf{x} - \boldsymbol{\mu}_i)}, \quad \boldsymbol{\Sigma}_i = \mathbf{R}_i \mathbf{S}_i \mathbf{S}_i^\top \mathbf{R}_i^\top. \quad (1)$$

where the scale matrix is defined as  $\mathbf{S}_i = \text{diag}(s_x, s_y, s_z)$ , with per-axis scales  $\mathbf{s}_i = [s_x, s_y, s_z]^\top \in \mathbb{R}^3$ . Each 3D Gaussian  $\mathbf{G}_i$  is projected onto the image plane as a 2D Gaussian  $\mathbf{G}_i^{2D}$  [33] using the camera intrinsics  $\mathbf{K}$  and camera pose  $\mathbf{T}^c \in \text{SE}(3)$ . The resulting 2D mean and covariance are given by  $\boldsymbol{\mu}_i^{2D} = \mathbf{K}(\mathbf{T}^c \boldsymbol{\mu}_i / (\mathbf{T}^c \boldsymbol{\mu}_i)_z)$ ,  $\boldsymbol{\Sigma}_i^{2D} = \mathbf{J}_i \mathbf{W} \boldsymbol{\Sigma}_i \mathbf{W}^\top \mathbf{J}_i^\top$ , where  $\mathbf{W}$  is the rotational component of  $\mathbf{T}^c$ , and  $\mathbf{J}_i$  denotes the Jacobian of the local projective transformation.

Sorting Gaussians front-to-back along the viewing ray, the color at pixel  $\mathbf{u}$  is

$$\mathbf{C}(\mathbf{u}) = \sum_{i=1}^N \mathbf{c}_i \alpha_i \mathbf{G}_i^{2D}(\mathbf{u}) \prod_{j=1}^{i-1} (1 - \alpha_j \mathbf{G}_j^{2D}(\mathbf{u})). \quad (2)$$

### B. Differentiable Camera Pose Rasterizer

Gaussian Splatting SLAM [34] extends the original 3DGS [2] rasterizer by enabling gradients to flow to the camera pose  $\mathbf{T}^c$  through an analytical Jacobian. Specifically, it optimizes the photometric loss  $\mathcal{L}$  with respect to  $\mathbf{T}^c$ . Each 3D Gaussian center  $\boldsymbol{\mu}_i \in \mathbb{R}^3$  is transformed into the camera

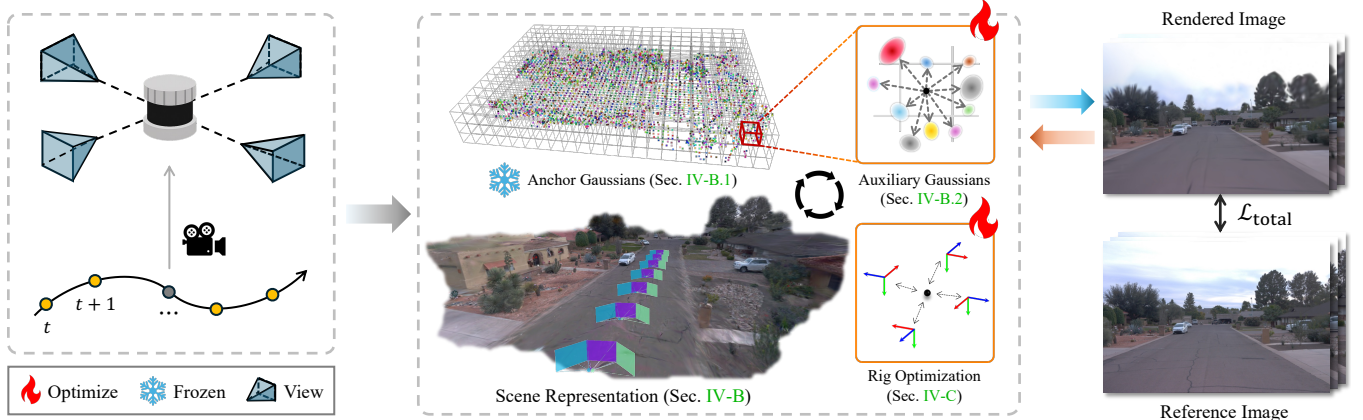


Fig. 2: Overview of the TLC-Calib pipeline. After aggregating LiDAR scans into a globally aligned point cloud, anchor Gaussians serve as fixed geometric references (their positions are not optimized), while auxiliary Gaussians adapt to local geometry and guide extrinsic optimization through photometric loss. Unlike anchor Gaussians, auxiliary Gaussians serve as learnable buffers around anchors, helping the optimization avoid local minima. Additionally, a rig-based optimization strategy jointly refines all cameras in relation to the scene, ensuring consistent and stable calibration across views.

coordinate frame as  $\mu_i^c = \mathbf{R}^c \mu_i + \mathbf{t}^c$ . The camera center in the world coordinate frame is given by  $\mathbf{o}_c = -(\mathbf{R}^c)^{-1} \mathbf{t}^c$ . Using the chain rule, the gradient of the loss with respect to the camera pose is expressed as:

$$\begin{aligned} \frac{\partial \mathcal{L}}{\partial \mathbf{T}^c} = \sum_i \left( \frac{\partial \mathcal{L}}{\partial \mu_i^{2D}} \frac{\partial \mu_i^{2D}}{\partial \mu_i^c} \frac{\partial \mu_i^c}{\partial \mathbf{T}^c} \right. \\ \left. + \frac{\partial \mathcal{L}}{\partial \Sigma_i^{2D}} \frac{\partial \Sigma_i^{2D}}{\partial \mathbf{T}^c} + \frac{\partial \mathcal{L}}{\partial \mathbf{c}_i} \frac{\partial \mathbf{c}_i}{\partial \mathbf{T}^c} \right), \end{aligned} \quad (3)$$

where  $\mu_i^{2D}$  is the projected center in the image. The Jacobian  $\frac{\partial \mu_i^c}{\partial \mathbf{T}^c}$ ,  $\frac{\partial \mathbf{c}_i}{\partial \mathbf{T}^c}$  and  $\frac{\partial \mathbf{o}_c}{\partial \mathbf{T}^c}$  follow standard rigid body transformation rules:

$$\begin{aligned} \frac{\partial \mu_i^c}{\partial \mathbf{T}^c} &= [\mathbf{I} \quad -[\mu_i^c]_{\times}], \\ \frac{\partial \mathbf{c}_i}{\partial \mathbf{T}^c} &= \frac{\partial \mathbf{c}_i}{\partial \mathbf{o}_c} \frac{\partial \mathbf{o}_c}{\partial \mathbf{T}^c}, \quad \frac{\partial \mathbf{o}_c}{\partial \mathbf{T}^c} = [\mathbf{0} \quad (\mathbf{R}^c)^{-1}]. \end{aligned} \quad (4)$$

The covariance matrix  $\Sigma_i^{2D}$  depends on the projection Jacobian  $\mathbf{J}_i$  and the camera rotation  $\mathbf{R}^c$ , leading to the gradient:

$$\frac{\partial \Sigma_i^{2D}}{\partial \mathbf{T}^c} = \frac{\partial \Sigma_i^{2D}}{\partial \mathbf{J}_i} \frac{\partial \mathbf{J}_i}{\partial \mu_i^c} \frac{\partial \mu_i^c}{\partial \mathbf{T}^c} + \frac{\partial \Sigma_i^{2D}}{\partial \mathbf{R}^c} \frac{\partial \mathbf{R}^c}{\partial \mathbf{T}^c}. \quad (5)$$

The derivative  $\frac{\partial \mathbf{R}^c}{\partial \mathbf{T}^c}$ , derived from the  $\text{SE}(3)$  group and using the standard basis vector  $\mathbf{e}_i \in \mathbb{R}^3$ , is given by  $\frac{\partial \mathbf{R}^c}{\partial \mathbf{T}^c} = [[\mathbf{e}_1] \times \mathbf{R}^c \quad [\mathbf{e}_2] \times \mathbf{R}^c \quad [\mathbf{e}_3] \times \mathbf{R}^c]$ . Following Matsuki *et al.* [34], the camera pose  $\mathbf{T}^c$  is updated on the  $\text{SE}(3)$  manifold via  $\mathbf{T}^c \leftarrow \exp(-\lambda \frac{\partial \mathcal{L}}{\partial \mathbf{T}^c}) \mathbf{T}^c$ , ensuring gradients respect the Lie group structure.

## IV. METHOD

### A. Overview

We propose a neural Gaussian-based approach for targetless calibration in a LiDAR and multi-camera setup. We adopt the LiDAR as the reference sensor, treating its coordinate frame as the global reference and calibrating all cameras relative

to it. This design choice is driven by the wide horizontal field of view and precise 3D geometry of LiDAR, which enables reliable odometry estimation through SLAM [35], ICP-based registration [36], or fusion with GPS and IMU for drift-free trajectories. Such multi-sensor fusion pipelines are widely adopted in autonomous driving datasets, including KITTI-360 [37] and WAYMO [38]. Building on this, we aggregate LiDAR point clouds over time using odometry, ensuring geometric consistency before calibration. In this work, we assume that LiDAR poses are given and that sensor timestamps are well synchronized. An overview of the proposed pipeline is shown in Fig. 2.

### B. Neural Scene Representation

1) *Anchor Gaussians*: Since the LiDAR serves as the reference sensor, we aggregate point clouds across timestamps  $t \in \{1, \dots, T\}$  to form  $\mathcal{P} = \bigcup_{t=1}^T \mathcal{P}_t$ , where  $\mathcal{P}_t$  denotes each LiDAR scan. We construct anchor Gaussians by voxelizing  $\mathcal{P}$  with an adaptively determined voxel size  $\varepsilon^*$  (Sec. IV-D). Each voxel center,

$$\mathbf{v}_i = \left\lfloor \frac{\mathbf{p}_j}{\varepsilon^*} \right\rfloor \cdot \varepsilon^*, \quad \mathbf{p}_j \in \mathcal{P}, \quad (6)$$

defines an anchor Gaussian that provides a consistent reference in real-world coordinates. This adaptive voxelization ensures that the anchor density automatically aligns with the spatial scale of the scene.

Our approach follows [39] but differs in that anchor positions remain fixed throughout training, with modifications tailored for LiDAR-camera calibration. Instead of refining anchor points, we adapt the anchor refinement process to retain their original positions, preserving scale and mitigating drift. Anchors with persistently low opacity, which typically arise from noise, are treated as floaters and removed during training.

TABLE I: Baseline comparison on KITTI-360 [37]. We report calibration accuracy (rotation in degrees, translation in meters) for the front and side cameras, along with optimization time. All results are averaged over the five test scenes. The **best**, **second-best**, and **third-best** results are highlighted in red, orange, and yellow, respectively.

Methods	Time↓	Front		Side	
		$R(^{\circ}) \downarrow$	$t(m) \downarrow$	$R(^{\circ}) \downarrow$	$t(m) \downarrow$
CalibAnything [24]	~5 hrs	2.820	0.386	4.993	0.746
NoPoseGS [29]	~10 min	5.071	0.973	2.269	0.484
INF [17]	~4 hrs	0.196	0.124	0.618	0.528
3DGS-Calib* [30]	~5 min	0.874	0.152	1.852	0.320
Ours	~10 min	0.128	0.093	0.149	0.094

2) *Auxiliary Gaussians*: While anchor Gaussians remain static, we introduce auxiliary Gaussians to refine local geometry and improve pose convergence. For each anchor  $\mathbf{v}_i$ , a lightweight MLP  $F_{\text{auxiliary}}$  predicts a set of positional offsets  $\boldsymbol{\delta}_i = \{\boldsymbol{\delta}_{i,1}, \dots, \boldsymbol{\delta}_{i,k}\}$ , conditioned on the anchor feature  $f_i$ , view-dependent input  $\mathbf{d}_{i,c}$ , and learned scale  $\ell_i$ . Each auxiliary Gaussian center  $\mathbf{m}_{i,k}$  is then defined by adding its offset to the corresponding anchor position:

$$\boldsymbol{\delta}_i = F_{\text{auxiliary}}(f_i, \mathbf{d}_{i,c}, \ell_i), \quad \mathbf{m}_{i,k} = \mathbf{v}_i + \boldsymbol{\delta}_{i,k}. \quad (7)$$

Other attributes such as covariance  $\Sigma_i$ , color  $\mathbf{c}_i$ , and opacity  $\alpha_i$  are decoded via separate MLPs conditioned on  $\{f_i, \mathbf{d}_{i,c}, \ell_i\}$ .

3) *Role of Auxiliary Gaussians*: Auxiliary Gaussians act as learnable buffers around anchors, allowing local geometry and appearance to adapt flexibly when sensor poses deviate from their initial estimates. In addition, they facilitate gradient flow in sparse or unobserved regions, such as the sky or the upper parts of buildings, by introducing trainable structures in areas lacking direct LiDAR observations.

This mechanism distinguishes our approach from the prior method [30], which regresses Gaussian attributes directly from LiDAR points using MLPs and is therefore constrained to observed regions (see Fig. 6 for comparison). Because rendering loss cannot propagate to areas without LiDAR coverage, this method often relies on image cropping to avoid untrained regions. In contrast, our auxiliary Gaussians expand spatial coverage while preserving global scale consistency, as they are derived from anchor features and absorb supervision from nearby pixels even in LiDAR-unobserved areas.

### C. Joint Optimization of Scene and Extrinsic

We denote the LiDAR-to-camera extrinsic transformation as  $\mathbf{T}^e$ . Given the scene representation described previously, we jointly optimize the 3D Gaussians  $\mathbf{G}$  and the extrinsic parameters  $\{\mathbf{T}_n^e\}_{n=1}^N$  corresponding to each of the  $N$  cameras.

Formally, the optimization objective is:

$$\min_{\mathbf{G}, \mathbf{T}_n^e} \sum_{n=1}^N \sum_{t=1}^T \mathcal{L}_{\text{total}} \left( (I'_{n,t}, I_{n,t}); \mathbf{G}, \mathbf{T}_n^e \right), \quad (8)$$

where  $I'_{n,t}$  is the rendered image (as in Eq. 2), and each camera  $n$  provides  $T$  observed images  $\{I_{n,1}, \dots, I_{n,T}\}$ . After updating the extrinsic parameters  $\mathbf{T}^e$  based on the  $t$ -th image

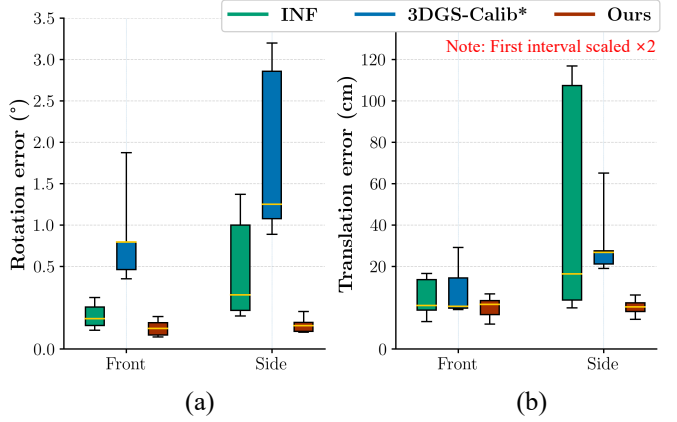


Fig. 3: Box plots of calibration accuracy: (a) rotation errors and (b) translation errors on KITTI-360 scenes over 10 trials. Our method consistently yields lower errors than the baselines for both front and side cameras, with particularly large improvements on side views. For clarity, the first y-axis interval is enlarged by a factor of two.

of a given camera, the same update is consistently applied to all images captured by that camera. This *camera rig optimization strategy* ensures internal consistency across the image set of each camera, thereby preserving the geometric alignment within the rig.

The pose update rule for an arbitrary camera is given by:

$$\mathbf{T}^e \leftarrow \mathbf{T}^e - \alpha \nabla_{\mathbf{T}^e} \sum_{t=1}^T \mathcal{L}_{\text{photo}} (I'_t, I_t), \quad (9)$$

where  $\alpha$  is the step size, and  $\mathcal{L}_{\text{photo}}$  denotes the photometric loss function, which is differentiable with respect to the camera pose, as described in Eq. 3.

### D. Adaptive Voxel Control

To balance spatial resolution and computational efficiency, we determine the voxel size  $\varepsilon^*$  by matching the downsampled point count to a target voxel number  $N_{\text{target}}$  via binary search:

$$\varepsilon^* = \arg \min_{\varepsilon} |N(\varepsilon) - N_{\text{target}}|. \quad (10)$$

Here,  $N_{\text{target}}$  is set proportional to the LiDAR trajectory distance,  $D_{\text{traj}} = \sum_{t=1}^{T-1} \|\mathbf{T}_{t+1}^L - \mathbf{T}_t^L\|_2$ , with a proportionality factor  $\beta$ . This formulation enables *adaptive voxel control* (AVC), which dynamically regulates the number of anchor Gaussians according to the overall scene scale. Importantly, AVC also influences calibration accuracy, where an excessively small  $\varepsilon^*$  leads to over-densified anchors that hinder optimization stability, while an excessively large  $\varepsilon^*$  reduces geometric coverage and degrades calibration precision.

### E. Loss Function

We define the total loss as a combination of photometric supervision and a regularization term:

$$\mathcal{L}_{\text{total}} = \lambda_{\text{photo}} \mathcal{L}_{\text{photo}} + \lambda_{\text{scale}} \mathcal{L}_{\text{scale}}. \quad (11)$$

TABLE II: NVS results on the KITTI-360 and WAYMO [38] datasets. We report the average PSNR, SSIM, and LPIPS metrics over test scenes. The **best**, **second-best**, and **third-best** results are highlighted in red, orange, and yellow, respectively.

Datasets	Dataset Calib.			NoPoseGS [29]			INF [17]			3DGS-Calib* [30]			Ours			
	PSNR↑	SSIM↑	LPIPS↓	PSNR↑	SSIM↑	LPIPS↓	PSNR↑	SSIM↑	LPIPS↓	PSNR↑	SSIM↑	LPIPS↓	PSNR↑	SSIM↑	LPIPS↓	
KITTI-360	Straight	26.29	0.85	0.08	19.12	0.66	0.31	25.45	0.83	0.11	25.65	0.84	0.10	26.50	0.86	0.08
	Small zigzag	27.13	0.89	0.07	18.55	0.70	0.28	24.21	0.83	0.13	26.56	0.88	0.09	27.39	0.90	0.07
	Large zigzag	26.87	0.86	0.09	17.66	0.65	0.33	26.27	0.85	0.10	22.82	0.78	0.18	27.18	0.87	0.09
	Small rotation	24.96	0.81	0.13	14.99	0.54	0.47	23.50	0.77	0.17	24.30	0.79	0.15	25.08	0.81	0.13
	Large rotation	25.77	0.83	0.11	18.07	0.61	0.35	22.80	0.76	0.17	24.55	0.80	0.14	26.02	0.84	0.10
Mean		26.20	0.85	0.10	17.68	0.63	0.35	24.45	0.81	0.14	24.77	0.82	0.13	26.43	0.85	0.09
WAYMO	Scene 81	27.81	0.88	0.13	28.41	0.88	0.12	28.08	0.88	0.12	28.64	0.89	0.11	29.06	0.89	0.11
	Scene 226	23.78	0.77	0.18	23.03	0.75	0.21	22.10	0.75	0.22	23.70	0.77	0.18	24.97	0.80	0.15
	Scene 362	25.99	0.87	0.11	25.00	0.85	0.15	20.89	0.78	0.24	26.65	0.88	0.09	27.08	0.89	0.09
	Mean	25.86	0.84	0.14	25.48	0.83	0.16	23.69	0.80	0.19	26.33	0.85	0.13	27.04	0.86	0.11

TABLE III: NVS results on the FAST-LIVO2 [40] handheld solid-state LiDAR dataset.

Scenes	Dataset Calib.			Ours		
	PSNR↑	SSIM↑	LPIPS↓	PSNR↑	SSIM↑	LPIPS↓
Building	22.13	<b>0.755</b>	0.172	<b>22.16</b>	0.754	<b>0.171</b>
Landmark	23.81	0.656	0.223	<b>23.99</b>	<b>0.660</b>	<b>0.220</b>
Sculpture	19.47	0.550	<b>0.224</b>	<b>19.56</b>	<b>0.553</b>	<b>0.224</b>

The photometric loss  $\mathcal{L}_{\text{photo}}$  follows [2], combining  $L1$  and  $DSSIM$  terms for image reconstruction. The regularization term  $\mathcal{L}_{\text{scale}}$  penalizes degenerate, highly anisotropic Gaussians by constraining their aspect ratios. It is applied only to Gaussians that pass the view frustum filter. Let  $\mathcal{V}$  be the set of valid Gaussians, with each  $\mathbf{s}_i \in \mathbb{R}^3$  representing scale along each axis. The loss is defined as:

$$\mathcal{L}_{\text{scale}} = \frac{1}{|\mathcal{V}|} \sum_{i \in \mathcal{V}} \max \left( \frac{\max(\mathbf{s}_i)}{\min(\mathbf{s}_i)} - \sigma, 0 \right), \quad (12)$$

where  $\sigma$  is a predefined threshold (see Sec. V-C). If  $|\mathcal{V}| = 0$ , the loss is set to zero. This term stabilizes training by softly constraining Gaussian shapes while allowing adaptation to local geometry.

## V. EXPERIMENTAL EVALUATION

### A. Dataset

We evaluate our method on two public autonomous driving datasets, KITTI-360 [37] and WAYMO [38], as well as one handheld dataset, FAST-LIVO2 [40]. KITTI-360 includes a spinning LiDAR, two front-facing perspective cameras, and two side-mounted fisheye cameras. Following prior work [37], we select five representative scenes: Straight, Small zigzag, Small rotation, Large zigzag, and Large rotation. WAYMO features a top-mounted spinning LiDAR and five perspective cameras covering the front and sides. FAST-LIVO2 consists of a solid-state LiDAR paired with a single perspective camera, with both sensors facing forward. For evaluation, we select three test scenes from each dataset: WAYMO (81, 226, 362) and FAST-LIVO2 (Building, Landmark, Sculpture).

### B. Experimental Setup

1) *Initialization*: Calibration studies typically focus on refining extrinsic parameters from corrupted initial estimates. To evaluate our method on three datasets, we follow the *from-LiDAR initialization* protocol [19], which provides coarse camera poses derived from LiDAR odometry and approximate camera rotations. For instance, in KITTI-360, the four cameras are roughly aligned with yaw angles of  $0^\circ$  (front),  $90^\circ$  (left), and  $-90^\circ$  (right). This initialization is challenging, as translation errors can reach up to 1.2m, substantially degrading calibration accuracy. As a result, existing targetless calibration methods often fail to converge under this setting.

2) *Baselines*: We compare our method against four baselines and the dataset-provided calibration, resulting in a total of five comparison methods. The baselines were selected according to three criteria: (1) public code availability, (2) relevance to targetless LiDAR–camera calibration, and (3) pose optimization based on 3DGS. Methods satisfying at least two of these criteria were chosen as baselines. We adopt these criteria because several related approaches [18], [19], [30] have not released their source code, making direct and reproducible comparison challenging.

Among the unreleased works, 3DGS-Calib [30] is the most relevant method, satisfying criteria (2) and (3). Since its official implementation is unavailable, we re-implemented it and used it as our primary baseline, denoted with an asterisk (\*). NoPoseGS [29], which meets criteria (1) and (3), provides public code and performs 3DGS-based pose optimization. We extended it to support LiDAR–camera calibration. The remaining baselines, CalibAnything [24] and INF [17], satisfy criteria (1) and (2) but do not natively support multi-camera LiDAR setups. Therefore, we modified both methods to operate in multi-camera configurations for fair comparison. Finally, the *dataset calibration*, obtained through target-based multi-sensor calibration with global bundle adjustment [37], serves as a reference for comparison.

### C. Implementation Details

We use a two-layer MLP with ReLU activation and 32 hidden units to regress Gaussian attributes. The parameters are set to  $K=5$ ,  $\beta=5000$ , and  $\sigma=10$  for the number of auxiliary Gaussians, the proportionality factor of  $N_{\text{target}}$ , and the scale



Fig. 4: Qualitative comparison on WAYMO. Key improvements are highlighted with yellow boxes, and cropped patches show zoomed-in regions for clarity. PSNR values of the rendered outputs are shown in the top-right corner of each image.

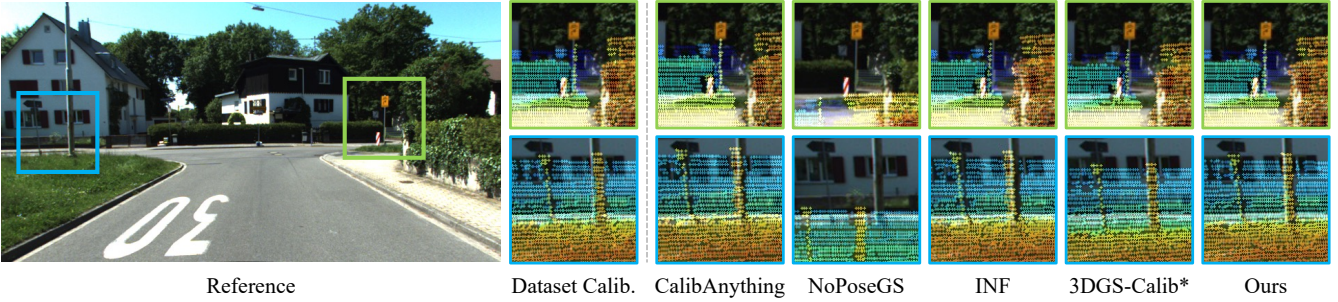


Fig. 5: Qualitative evaluation of LiDAR-camera alignment accuracy with KITTI-360 dataset. LiDAR points are projected onto images using the calibration results estimated by each baseline method. Point colors indicate 3D distances from the LiDAR, ranging from red (near) to blue (far).

regularization threshold, respectively. Training is conducted for 30K iterations using AdamW, with a weight decay of  $10^{-2}$  applied for the first 15K iterations. To enhance calibration stability, each camera has a separate optimizer with learning rates of  $2 \times 10^{-3}$  for rotation and  $8 \times 10^{-3}$  for translation. The loss combines  $D\text{-SSIM}$  and scale terms, weighted by  $\lambda_{D\text{-SSIM}}=0.2$  and  $\lambda_{\text{scale}}=1.0$ . All experiments were conducted on a single RTX 4090 GPU, except 3DGS-Calib\* [30], which required an RTX 5090 due to OOM. Our method remained below 8GB of VRAM and utilized the *same hyperparameters* for all datasets.

#### D. Evaluation of Calibration Accuracy

Calibration accuracy is evaluated by comparing the estimated extrinsics of each method with the *dataset calibration*. Rotation error( $^\circ$ ) and translation error(m) are used as evaluation metrics. Tab. I summarizes the KITTI-360 [37] results, where our method achieves the lowest errors. For both front and side cameras, the average rotation error remains around  $0.1^\circ$ , effectively reducing large projection deviations caused by small angular misalignments. Fig. 5 visualizes the alignment quality, showing that our method preserves

accurate registration even for distant objects.

The KITTI-360 dataset features front-view perspective and side-mounted fisheye cameras, requiring consistent alignment across wide viewing angles and large distortions. Nevertheless, our method maintains high accuracy across all camera types (rotation error:  $0.138^\circ$ , translation error: 0.094m) by jointly optimizing camera poses within a shared scene space and leveraging structural constraints. In contrast, baseline methods [17], [30] exhibit unstable convergence depending on hyperparameter settings and scene complexity. As shown in Fig. 3, they produce larger variance in both rotation and translation errors. Since the WAYMO dataset [38] provides less reliable calibration and pose information [41], we evaluate calibration quality based on NVS performance, which strongly reflects the accuracy of estimated extrinsics.

#### E. Evaluation of Novel View Synthesis

Novel View Synthesis (NVS) quality is evaluated using PSNR, SSIM [42], and LPIPS [43]. For each baseline method, we first obtain the estimated extrinsics and apply them to a 3DGS [2] pipeline, which has been modified to utilize LiDAR point clouds instead of SfM-based points for initialization. It

TABLE IV: Ablation study of different model components. AVC denotes adaptive voxel control, and R-O denotes rig optimization.

Models	Accuracy		Novel View Synthesis		
	$\mathbf{R}(\circ) \downarrow$	$t(\text{m}) \downarrow$	PSNR $\uparrow$	SSIM $\uparrow$	LPIPS $\downarrow$
<b>Full</b>	<b>0.138</b>	<b>0.094</b>	<b>26.43</b>	<b>0.854</b>	<b>0.094</b>
w/o $\mathcal{L}_{\text{scale}}$	0.223	0.125	26.00	0.844	0.104
w/o AVC	0.284	0.158	25.72	0.837	0.109
w/o R-O	1.944	0.452	22.54	0.750	0.199

TABLE V: Ablation study on extrinsic parameter generalization. Calibration optimized on **Scene A** is applied to **Scene B** and **Scene C**, and evaluated using NVS metrics.

Scenes	Dataset Calib.			Ours		
	PSNR $\uparrow$	SSIM $\uparrow$	LPIPS $\downarrow$	PSNR $\uparrow$	SSIM $\uparrow$	LPIPS $\downarrow$
Seq. 9A	26.87	0.864	0.092	<b>27.18</b>	<b>0.866</b>	<b>0.091</b>
Seq. 9B	26.21	0.866	<b>0.089</b>	<b>26.31</b>	<b>0.867</b>	0.089
Seq. 9C	24.01	0.829	0.120	<b>24.16</b>	<b>0.831</b>	<b>0.118</b>
Seq. 10A	24.96	0.810	0.130	<b>25.08</b>	<b>0.811</b>	<b>0.129</b>
Seq. 10B	24.04	0.814	0.124	<b>24.17</b>	<b>0.816</b>	<b>0.124</b>
Seq. 10C	23.74	0.832	<b>0.100</b>	<b>23.77</b>	<b>0.832</b>	0.101

is necessary because all baselines estimate the poses between LiDAR and cameras, not the full camera trajectories that SfM typically provides. Since high-quality novel view synthesis inherently depends on precise camera parameters [44], we use NVS performance as a reliable indicator of calibration accuracy beyond the *dataset calibration*.

As shown in Tab. II, our method achieves the highest rendering quality across all scenes in KITTI-360 and WAYMO. On WAYMO, both TLC-Calib and 3DGS-Calib\* outperform the dataset calibration, whereas on KITTI-360, only our method surpasses it. Fig. 4 further demonstrates sharper reconstruction and better rendering consistency compared to both baselines and the dataset calibration. Finally, to validate generalization across different sensor configurations, we evaluate our method on a solid-state LiDAR setup, where it slightly outperforms the dataset calibration in NVS metrics (Tab. III).

#### F. Ablation Study

1) *Model Components*: We evaluate the contribution of each model component through ablation experiments (Tab. IV). The scale loss  $\mathcal{L}_{\text{scale}}$  regularizes Gaussians from becoming overly sharp or elongated, thereby improving calibration stability. Adaptive voxel control (AVC) dynamically adjusts voxel sizes according to the scene scale, leading to more reliable initialization and higher accuracy compared to the fixed-size setting ( $\epsilon = 0.1$ , “w/o AVC”). Finally, rig-based optimization (R-O) significantly accelerates convergence under noisy *from-LiDAR* initialization and enhances overall robustness. As summarized in Tab. IV, removing any of these components results in notable performance degradation. In particular, disabling R-O leads to severe degradation, increasing the translation error from 0.094m to 0.452m.

2) *Extrinsic Generalization*: To further assess generalization, we apply the extrinsics optimized on **Scene A** to novel

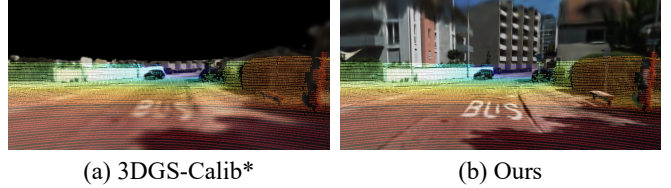


Fig. 6: Scene representation comparison. Rendering results during training: (a) 3DGS-Calib\* and (b) Ours. Initial LiDAR points are overlaid and color-coded by distance. Our method reconstructs upper regions, whereas (a) fails to render these areas due to image cropping.

TABLE VI: Ablation study on image cropping. Calibration accuracy and NVS results are reported for 3DGS-Calib\*, ours with cropping, and our full model.

Models	Accuracy		Novel View Synthesis		
	$\mathbf{R}(\circ) \downarrow$	$t(\text{m}) \downarrow$	PSNR $\uparrow$	SSIM $\uparrow$	LPIPS $\downarrow$
3DGS-Calib* [30]	1.363	0.236	24.78	0.816	0.131
TLC-Calib w/ crop	0.300	0.393	26.02	0.844	0.104
TLC-Calib (Ours)	<b>0.138</b>	<b>0.094</b>	<b>26.43</b>	<b>0.854</b>	<b>0.094</b>

Scene B and Scene C without recalibration. A key indicator of calibration quality is whether the estimated extrinsics remain effective when transferred across sequences captured by the same vehicle. Here, Seq. 9A (Large zigzag) and Seq. 10A (Small rotation) serve as source scenes, while 9B/C and 10B/C are their corresponding targets within the same KITTI-360 sequence. As shown in Tab. V, our method achieves consistently higher NVS metrics on the target scenes than the default dataset calibration, demonstrating strong cross-scene calibration robustness.

3) *Image Cropping*: We further analyze the effect of image cropping on calibration accuracy. As described in Sec. IV-B.3, the previous Gaussian-based approach [30] crops the upper half of the image based on the LiDAR configuration, as that region usually lacks LiDAR measurements. However, this assumption fails under different sensor configurations (e.g., varying FOVs, or handheld setups), limiting its generalization. As reported in Tab. VI, applying a crop ratio of 0.5 notably degrades calibration accuracy due to the reduced image information. In contrast, our method maintains robustness without image cropping by leveraging auxiliary Gaussians to handle regions unobserved by LiDAR. Fig. 6 compares intermediate renderings, where our approach successfully reconstructs upper regions.

## VI. CONCLUSION

In this paper, we introduced TLC-Calib, a targetless LiDAR-camera calibration framework that leverages neural scene representation without scene-specific hyperparameters. Our method jointly optimizes scene representation and sensor poses using neural Gaussians, whose geometric consistency mitigates viewpoint overfitting and improves convergence stability. Experiments on two public driving datasets and one handheld dataset demonstrate superior pose accuracy,

rendering quality, and scene generalization compared to existing methods. Future work includes incorporating LiDAR rendering for joint multi-LiDAR optimization and extending the framework to time calibration and dynamic scenes.

## REFERENCES

- [1] B. Mildenhall, P. P. Srinivasan, M. Tancik, J. T. Barron, R. Ramamoorthi, and R. Ng, “Nerf: Representing scenes as neural radiance fields for view synthesis,” in *Eur. Conf. Comput. Vis. (ECCV)*. Springer, 2020, pp. 405–421.
- [2] B. Kerbl, G. Kopanas, T. Leimkühler, and G. Drettakis, “3d gaussian splatting for real-time radiance field rendering,” *ACM Trans. Graph. (ToG)*, vol. 42, no. 4, pp. 139–1, 2023.
- [3] M. Levoy and P. Hanrahan, “Light field rendering,” in *Proceedings of the 23rd Annual Conference on Computer Graphics and Interactive Techniques*, ser. SIGGRAPH ’96. Association for Computing Machinery, 1996, p. 31–42.
- [4] S. J. Gortler, R. Grzeszczuk, R. Szeliski, and M. F. Cohen, “The lumigraph,” in *Proceedings of the 23rd Annual Conference on Computer Graphics and Interactive Techniques*, ser. SIGGRAPH ’96. Association for Computing Machinery, 1996, p. 43–54.
- [5] C. Zhao, S. Sun, R. Wang, Y. Guo, J.-J. Wan, Z. Huang, X. Huang, Y. V. Chen, and L. Ren, “TCLC-GS: Tightly Coupled LiDAR-Camera Gaussian Splatting for Autonomous Driving,” in *Eur. Conf. Comput. Vis. (ECCV)*, 2024, p. 91–106.
- [6] Z. Chen, J. Yang, J. Huang, R. de Lutio, J. M. Esturo, B. Ivanovic, O. Litany, Z. Gojcic, S. Fidler, M. Pavone, L. Song, and Y. Wang, “OmniRe: Omni Urban Scene Reconstruction,” in *Int. Conf. Learn. Represent. (ICLR)*, 2025.
- [7] Q. Zhang and R. Pless, “Extrinsic calibration of a camera and laser range finder,” in *IEEE/RSJ Int. Conf. on Intelligent Robots and Systems (IROS)*, vol. 3. IEEE, 2004, pp. 2301–2306.
- [8] A. Geiger, F. Moosmann, Ö. Car, and B. Schuster, “Automatic camera and range sensor calibration using a single shot,” in *IEEE Int. Conf. on Robotics and Automation (ICRA)*. IEEE, 2012, pp. 3936–3943.
- [9] F. M. Mirzaei, D. G. Kottas, and S. I. Roumeliotis, “3D LiDAR-camera intrinsic and extrinsic calibration: Identifiability and analytical least-squares-based initialization,” *The International Journal of Robotics Research*, vol. 31, no. 4, pp. 452–467, 2012.
- [10] J. Levinson and S. Thrun, “Automatic online calibration of cameras and lasers,” in *Robotics: Science and Systems*, vol. 2, no. 7. Citeseer, 2013.
- [11] D. Scaramuzza, A. Harati, and R. Siegwart, “Extrinsic self calibration of a camera and a 3D laser range finder from natural scenes,” in *IEEE/RSJ Int. Conf. on Intelligent Robots and Systems (IROS)*. IEEE, 2007, pp. 4164–4169.
- [12] M. Á. Muñoz-Bañón, F. A. Candelas, and F. Torres, “Targetless camera-lidar calibration in unstructured environments,” *IEEE Access*, vol. 8, pp. 143 692–143 705, 2020.
- [13] N. Schneider, F. Piewak, C. Stiller, and U. Franke, “RegNet: Multimodal sensor registration using deep neural networks,” in *IEEE Intelligent Vehicles Symposium*. IEEE, 2017, pp. 1803–1810.
- [14] X. Lv, B. Wang, Z. Dou, D. Ye, and S. Wang, “LCCNet: LiDAR and camera self-calibration using cost volume network,” in *IEEE Conf. Comput. Vis. Pattern Recog. Worksh. (CVPRW)*, 2021, pp. 2888–2895.
- [15] W. Sun, E. Trulls, Y.-C. Tseng, S. Sambandam, G. Sharma, A. Tagliasacchi, and K. M. Yi, “PointNeRF++: a multi-scale, point-based neural radiance field,” in *Eur. Conf. Comput. Vis. (ECCV)*. Springer, 2024, pp. 221–238.
- [16] J. Deng, Q. Wu, X. Chen, S. Xia, Z. Sun, G. Liu, W. Yu, and L. Pei, “Nerf-loam: Neural implicit representation for large-scale incremental lidar odometry and mapping,” in *Int. Conf. Comput. Vis. (ICCV)*, 2023, pp. 8218–8227.
- [17] S. Zhou, S. Xie, R. Ishikawa, K. Sakurada, M. Onishi, and T. Oishi, “Inf: Implicit neural fusion for lidar and camera,” in *IEEE/RSJ Int. Conf. on Intelligent Robots and Systems (IROS)*. IEEE, 2023, pp. 10918–10925.
- [18] Q. Herau, N. Piasco, M. Bennehar, L. Roldão, D. Tsishkou, C. Mignot, P. Vasseur, and C. Demonceaux, “MOISST: Multimodal Optimization of Implicit Scene for SpatioTemporal Calibration,” in *IEEE/RSJ Int. Conf. on Intelligent Robots and Systems (IROS)*. IEEE, 2023, pp. 1810–1817.
- [19] Z. Yang, G. Chen, H. Zhang, K. Ta, I. A. Bârsan, D. Murphy, S. Manivasagam, and R. Urtasun, “UniCal: Unified Neural Sensor Calibration,” in *Eur. Conf. Comput. Vis. (ECCV)*. Springer, 2024, pp. 327–345.
- [20] X. Zhang, S. Zhu, S. Guo, J. Li, and H. Liu, “Line-based automatic extrinsic calibration of LiDAR and camera,” in *IEEE Int. Conf. on Robotics and Automation (ICRA)*. IEEE, 2021, pp. 9347–9353.
- [21] S. Wang, X. Zhang, G. Zhang, Y. Xiong, G. Tian, S. Guo, J. Li, P. Lu, J. Wei, and L. Tian, “Temporal and spatial online integrated calibration for camera and LiDAR,” in *IEEE International Conference on Intelligent Transportation Systems*. IEEE, 2022, pp. 3016–3022.
- [22] Y. Zhu, C. Li, and Y. Zhang, “Online camera-lidar calibration with sensor semantic information,” in *IEEE Int. Conf. on Robotics and Automation (ICRA)*. IEEE, 2020, pp. 4970–4976.
- [23] P. Rotter, M. Klemiato, and P. Skruch, “Automatic calibration of a lidar-camera system based on instance segmentation,” *Remote Sensing*, vol. 14, no. 11, p. 2531, 2022.
- [24] Z. Luo, G. Yan, X. Cai, and B. Shi, “Zero-training LiDAR-Camera Extrinsic Calibration Method Using Segment Anything Model,” in *IEEE Int. Conf. on Robotics and Automation (ICRA)*, 2024, pp. 14 472–14 478.
- [25] Z. Wang, S. Wu, W. Xie, M. Chen, and V. A. Prisacariu, “NeRF—: Neural radiance fields without known camera parameters,” *arXiv preprint arXiv:2102.07064*, 2021.
- [26] Y. Jeong, S. Ahn, C. Choy, A. Anandkumar, M. Cho, and J. Park, “Self-calibrating neural radiance fields,” in *Int. Conf. Comput. Vis. (ICCV)*, 2021, pp. 5846–5854.
- [27] W. Bian, Z. Wang, K. Li, J.-W. Bian, and V. A. Prisacariu, “Nope-nerf: Optimising neural radiance field with no pose prior,” in *IEEE Conf. Comput. Vis. Pattern Recog. (CVPR)*, 2023, pp. 4160–4169.
- [28] Y. Fu, S. Liu, A. Kulkarni, J. Kautz, A. A. Efros, and X. Wang, “COLMAP-Free 3D Gaussian Splatting,” in *IEEE Conf. Comput. Vis. Pattern Recog. (CVPR)*, June 2024, pp. 20 796–20 805.
- [29] C. Schmidt, J. Piekenbrinck, and B. Leibe, “Look Gauss, No Pose: Novel View Synthesis using Gaussian Splatting without Accurate Pose Initialization,” in *IEEE/RSJ Int. Conf. on Intelligent Robots and Systems (IROS)*, 2024, pp. 8732–8739.
- [30] Q. Herau, M. Bennehar, A. Moreau, N. Piasco, L. Roldão, D. Tsishkou, C. Mignot, P. Vasseur, and C. Demonceaux, “3DGS-Calib: 3D Gaussian Splatting for Multimodal SpatioTemporal Calibration,” in *IEEE/RSJ Int. Conf. on Intelligent Robots and Systems (IROS)*, 2024, pp. 8315–8321.
- [31] T. Müller, A. Evans, C. Schied, and A. Keller, “Instant neural graphics primitives with a multiresolution hash encoding,” *ACM Trans. Graph. (ToG)*, vol. 41, no. 4, pp. 1–15, 2022.
- [32] S. Zhou, S. Xie, R. Ishikawa, and T. Oishi, “Robust LiDAR-Camera Calibration With 2D Gaussian Splatting,” *IEEE Robotics and Automation Letters*, 2025.
- [33] M. Zwicker, H. Pfister, J. Van Baar, and M. Gross, “EWA splatting,” *IEEE Trans. Vis. Comput. Graph. (TVCG)*, vol. 8, no. 3, pp. 223–238, 2002.
- [34] H. Matsuki, R. Murai, P. H. Kelly, and A. J. Davison, “Gaussian splatting slam,” in *IEEE Conf. Comput. Vis. Pattern Recog. (CVPR)*, 2024, pp. 18 039–18 048.
- [35] Z. Chen, Y. Xu, S. Yuan, and L. Xie, “ig-lio: An incremental gicp-based tightly-coupled lidar-inertial odometry,” *IEEE Robotics and Automation Letters*, vol. 9, no. 2, pp. 1883–1890, 2024.
- [36] I. Vizzo, T. Guadagnino, B. Mersch, L. Wiesmann, J. Behley, and C. Stachniss, “Kiss-icp: In defense of point-to-point icp-simple, accurate, and robust registration if done the right way,” *IEEE Robotics and Automation Letters*, vol. 8, no. 2, pp. 1029–1036, 2023.
- [37] Y. Liao, J. Xie, and A. Geiger, “Kitti-360: A novel dataset and benchmarks for urban scene understanding in 2d and 3d,” *IEEE Trans. Pattern Anal. Mach. Intell. (TPAMI)*, vol. 45, no. 3, pp. 3292–3310, 2022.
- [38] P. Sun, H. Kretzschmar, X. Dotiwalla, A. Chouard, V. Patnaik, P. Tsui, J. Guo, Y. Zhou, Y. Chai, B. Caine, et al., “Scalability in perception for autonomous driving: Waymo open dataset,” in *IEEE Conf. Comput. Vis. Pattern Recog. (CVPR)*, 2020, pp. 2446–2454.
- [39] T. Lu, M. Yu, L. Xu, Y. Xiangli, L. Wang, D. Lin, and B. Dai, “Scaffoldgs: Structured 3d gaussians for view-adaptive rendering,” in *IEEE Conf. Comput. Vis. Pattern Recog. (CVPR)*, 2024, pp. 20 654–20 664.
- [40] C. Zheng, W. Xu, Z. Zou, T. Hua, C. Yuan, D. He, B. Zhou, Z. Liu, J. Lin, F. Zhu, et al., “Fast-livo2: Fast, direct lidar-inertial-visual odometry,” *IEEE Transactions on Robotics*, 2024.

- [41] Q. Herau, N. Piasco, M. Bennehar, L. Roldão, D. Tsishkou, B. Liu, C. Mignot, P. Vasseur, and C. Demonceaux, “Pose optimization for autonomous driving datasets using neural rendering models,” *arXiv preprint arXiv:2504.15776*, 2025.
- [42] Z. Wang, A. Bovik, H. Sheikh, and E. Simoncelli, “Image quality assessment: from error visibility to structural similarity,” *IEEE Transactions on Image Processing*, vol. 13, no. 4, pp. 600–612, 2004.
- [43] R. Zhang, P. Isola, A. A. Efros, E. Shechtman, and O. Wang, “The Unreasonable Effectiveness of Deep Features as a Perceptual Metric,” in *IEEE Conf. Comput. Vis. Pattern Recog. (CVPR)*, 2018.
- [44] E. Brachmann, J. Wynn, S. Chen, T. Cavallari, A. Monzpart, D. Turmukhambetov, and V. A. Prisacariu, “Scene coordinate reconstruction: Posing of image collections via incremental learning of a relocizer,” in *European Conference on Computer Vision*. Springer, 2024, pp. 421–440.